Kinematics of nonlinear waves over variable bathymetry. Part II: Statistical distributions of orbital velocities and accelerations in irregular long-crested seas

Jie Zhang, Yuxiang Ma, Michel Benoit

Kinematics of nonlinear waves over variable bathymetry. Part II: Statistical distributions of orbital velocities and accelerations in irregular long-crested seas

Jie Zhang[a,b,*], Yuxiang Ma[c] and Michel Benoit[d,e]

[a]Qingdao Innovation and Development Base, Harbin Engineering University, Qingdao 266400, PR China
[b]Qingdao Innovation and Development Center of Harbin Engineering University, Qingdao 266400, PR China
[c]State Key Laboratory of Coastal and Offshore Engineering, Dalian University of Technology, Dalian 116023, PR China
[d]EDF R&D, Laboratoire National d'Hydraulique et Environnement (LNHE), Chatou, France
[e]LHSV, Saint -Venant Hydraulics Laboratory (Ecole des Ponts, EDF R&D), Chatou, France

ARTICLE INFO

Keywords:
Coastal waves
Nonlinear waves
Wave kinematics
Numerical simulation
Statistical distribution

ABSTRACT

In coastal areas, variable bottom effects significantly enhance wave nonlinearity and complicate wave propagation. It is of practical interest to characterize the nonlinear effect on the statistics of free surface displacements and particle kinematics. In this work, we take advantage of a fully nonlinear potential flow model to investigate the statistics of unidirectional irregular waves propagating over an uneven bottom. By confronting the simulated results with existing experimental results (free surface elevation and horizontal velocity beneath the mean sea level) in the temporal, spectral, and statistical domains, we show the high fidelity of the model in predicting the nonlinear irregular wave kinematics. As the relative importance of low-frequency harmonics becomes lower for acceleration, the model performance in predicting the measured horizontal acceleration is even better than that for the measured horizontal velocity. The empirical statistical distributions of velocity and acceleration in both horizontal and vertical directions are compared with both the normal (Gaussian) and the log-normal (LN) distributions. The latter requires skewness as an input in addition to the mean and standard deviation of the signal. We notice that, unlike the free surface displacement generally of positive skewness, the signal of velocities and accelerations are sometimes characterized by negative skewness. In such cases, the negative LN distribution should be adopted. Although the LN distribution has rarely been used for short-term statistics of wave elevation and kinematics, the detailed comparisons presented here demonstrate very good performance for all kinematic variables. In particular, in the area following a rapid reduction of water depth, where the sea-state is out-of-equilibrium, the heavy tails in the distributions are well reproduced by the LN model, indicating some generality and merits of this model.

1. Introduction

The statistics of Wave kinematics is of great importance in coastal and ocean engineering. For ships and offshore structures, it is keenly related to wave-induced forces (Kriebel, 1998; Wilson, 2002; Goda, 2010) while in coastal areas, it is relevant to the prediction of bottom shear stress, scour, and deposit of sediments. Wave kinematics is one of the key factors dominating the topography evolution, especially in coastal estuaries and along shorelines (Fredsøe and Deigaard, 1992; Elfrink and Baldock, 2002; Ostrowski et al., 2018). In the transition areas between offshore and coastal regions, as bottom effects get more and more involved, waves are subject to refraction, reflection, shoaling, and dissipation induced by bottom friction. The wave nonlinearity is gradually enhanced due to the reduction of water depth (Freilich and Guza, 1984), eventually, depth-limited breaking occurs in the surf zone. Recent studies show that, if the depth transition is sufficiently rapid and the relative water depth after depth change is below $k_p h < 1.3$ (with k_p denoting the wave number corresponding to the spectral peak frequency and h the water depth), the waves are dominated by the so-called non-equilibrium dynamics after shoaling, as argued in Trulsen et al. (2012, 2020). The non-equilibrium dynamics is, in essence, the interaction of bound and free superharmonics excited by the depth change (Li et al., 2021). Out-of-equilibrium sea-states are characterized by rapid spectral evolution, local and distinct non-Gaussian statistics, and intensified freak wave occurrence probability (see e.g. Zhang et al., 2019; Zheng et al., 2020; Bonar et al., 2021; Zhang and Benoit, 2021; Lawrence et al., 2021, 2022). Furthermore, in the context of global warming, coastal and ocean engineering is faced with extreme events becoming more frequent and challenging than ever (see e.g. Didenkulova and Pelinovsky, 2016, 2020; Didenkulova et al., 2023; Shi et al., 2024). Consequently, a better understanding and statistical/deterministic prediction of the strongly nonlinear free surface displacement and the flow field underneath remain of paramount importance (Zelt et al., 1995; Stansberg et al., 1995; Aggarwal et al., 2016; Vested et al., 2020; Li et al., 2023; Deng et al., 2023).

For linear sea-states, the irregular wave train is assumed to be the sum of an infinite number of statistically independent harmonic components with random phases. According

*Corresponding author
jie.zhang@hrbeu.edu.cn (J. Zhang); yuxma@dlut.edu.cn (Y. Ma); michel.benoit@edf.fr (M. Benoit)
ORCID(s): 0000-0003-0794-2335 (J. Zhang); 0000-0003-4314-0428 (Y. Ma); 0000-0003-4195-2983 (M. Benoit)

to the central limit theorem, the probability density function (PDF) of the free surface elevation (FSE), the orbital velocities and accelerations underneath all follow the Gaussian (G) distribution (Longuet-Higgins, 1952; You, 2009). For nonlinear sea-states, the nonlinearity modifies the statistics of FSE and leads to deviations from Gaussianity. Various approaches have been put forward to take these nonlinear effects into account in the FSE distribution, such as the asymptotic approach based on Stokes expansion which can be extended to high order within the validity range of the Stokes theory (Tayfun and Alkhalidi, 2020; Fuhrman et al., 2023; Klahn et al., 2024); the transformed Gaussian method which models the non-Gaussian FSE distribution using the knowledge associated with the Gaussian processes (Ochi and Wang, 1984; Socquet-Juglard et al., 2005; Winterstein and Haver, 2015); and the moment-based approach which build the FSE models based on the first three or four cumulants of the random process. The distribution model in Edgeworth's form of the Gram-Charlier (G–C) series (Longuet-Higgins, 1963), the Gamma model (Bolles et al., 2019), the exponential Gamma model (Herrman et al., 1997; Kobayashi et al., 1998), and the log-normal (LN) distribution (Zhang et al., 2024) belong to this third category. In Zhang et al. (2024), the LN distribution has been extensively compared with six models of different types for the FSE distribution, showing advantages in capturing the heavy tails in the empirical PDF of FSE. As for FSE, nonlinearity also results in deviations in the statistics of kinematics from Gaussianity. However, studies about non-Gaussian velocity and acceleration distributions are relatively limited. The G–C type model was adopted to describe the non-Gaussianity of the distribution of orbital velocity, but its performance fluctuates depending on the data set (Sultan and Hughes, 1993; Song and Wu, 2000). Considering the non-equilibrium statistics after a rapid depth variation, the discussion on the characteristics of kinematics statistics is rather scant, particularly due to the lack of high-quality and long-duration time series of either measured or simulated kinematic variables.

In the companion Part I article (Benoit et al., 2024) (hereafter referred to as BZM2024 for brevity), we have detailed the computation of wave kinematics within the framework of the fully nonlinear potential flow (FNPF) code Whispers3D (W3D). The numerical implementation has been verified by comparing the simulated kinematics of strongly nonlinear regular waves with the corresponding stream function solution and validated against experimental results of regular waves propagating over an uneven bottom. After providing further validation of the numerical code for computing the kinematics of strongly nonlinear irregular waves over an uneven bottom, the main target of this work is to test the applicability of the LN distribution to wave kinematics. Indeed, the LN model has been shown in Zhang et al. (2024) to be appropriate for the distribution of FSE. However, to the limit of our knowledge, the LN distribution has never been employed for describing the non-equilibrium statistics of particle kinematics in strongly variable seabed conditions.

The remainder of this article is organized as follows: In section 2, the W3D numerical computation of wave kinematics is further validated for nonlinear irregular waves propagating over a variable seabed. Comparing simulation results with experimental measurements, we show and discuss the time series of the horizontal velocity and acceleration, the evolution of the corresponding spectra, and statistical moments. Section 3 presents the statistical distributions of FSE, the horizontal and vertical components of the velocity and acceleration. The empirical (measured and simulated) distributions are compared with the G and the LN models. Conclusions and perspectives are provided in section 4.

2. Experimental validation for irregular nonlinear wave kinematics in variable water depth

2.1. Experimental configuration

In this section, an experimental case with irregular unidirectional waves propagating in variable water depth reported in Trulsen et al. (2020) is simulated, and we focus on the characteristics of particle kinematics. The experiments were performed in the University of Oslo (Norway) hydrodynamics laboratory. The sketch of the bathymetry is displayed in Fig. 1. The submerged bar is installed 10.78 m away from the piston-type wavemaker and consists of upslope, bar crest, and downslope sections, each of 1.6 m in length. The water depth in the deeper flat regions is $h_1 = 0.53$ m, and that over the bar is $h_2 = 0.11$ m. A series of non-breaking irregular wave configurations were tested during the experimental campaign. In Zhang and Benoit (2021), run 3 has been simulated using W3D, with analyses of the FSE and horizontal velocity presented. In the present work, we adopt the numerical method introduced in BZM2024 to directly evaluate the particle velocity and acceleration in both horizontal and vertical directions, and further discuss the spectral and statistical properties of velocity and acceleration.

Incident wave conditions of Run 3 are defined by a JONSWAP spectrum:

$$S(f) = \frac{\alpha g^2}{(2\pi)^4}\frac{1}{f^5}\exp\left[-\frac{5}{4}\left(\frac{f_p}{f}\right)^4\right]\gamma^{\exp\left[-\frac{1}{2}\left(\frac{f-f_p}{\sigma_J f_p}\right)^2\right]}, \quad (1)$$

where α controls the significant wave height H_s, f_p is the peak frequency, and σ_J is the asymmetry parameter, $\sigma_J = 0.07$ for $f < f_p$ and $\sigma_J = 0.09$ for $f > f_p$. The peak enhancement factor $\gamma = 3.3$ was fixed during the experimental campaign, the peak period is $T_p = 1/f_p = 1.1$ s, and the incident significant wave height is $H_s = 0.025$ m. In this configuration, the non-dimensional parameters offshore of the bar read: relative depth $\mu_1 = k_p h = 1.85$, wave steepness $\epsilon_1 = k_p a_c = 0.031$, and Ursell number $Ur_1 = \epsilon/\mu^3 = 0.005$, where k_p denotes the wave number corresponding to T_p and $a_c = H_s/\sqrt{8}$ the characteristic wave amplitude. Over the bar crest, $\mu_2 = 0.64$, $\epsilon_2 = 0.052$, and $Ur_2 = 0.192$.

The FSE η was measured at 91 positions with sampling frequency $f_s = 125$ Hz; the horizontal velocity $u(z_0)$ was

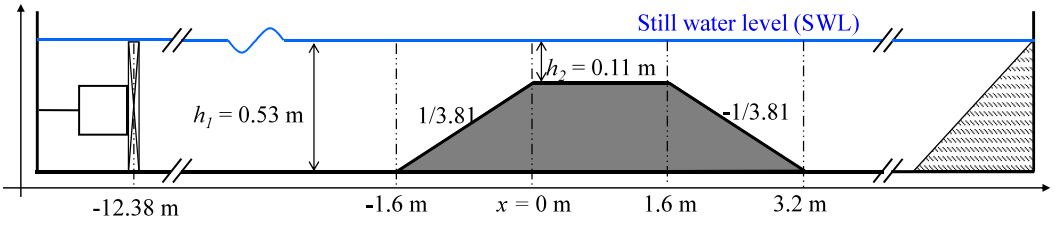

Figure 1: Sketch of the bathymetry used in the experiments reported in Trulsen et al. (2020)

measured with an acoustic Doppler velocimeter (ADV) device at 37 positions at the elevation $z_0 = -0.048$ m below the still water level (SWL), with a sampling frequency $f_s = 200$ Hz. Due to the limited number of measurement devices, the results were gathered by repeating the same experiment several times. In each repetition, the experiment lasted for 90 min, which represents a series of about 5000 waves with peak period T_p.

2.2. Numerical model setup

The implementation of the kinematics computation within the W3D model has been detailed in the part I paper and will not be duplicated here. In the current scenario, waves were generated and damped using relaxation zones of $3L_p = 5.4$ m length located at both ends of the flume, with $L_p \approx 1.80$ m denoting the wavelength corresponding to T_p in water depth h_1. The space and time are discretized with constant intervals, $\Delta x = 0.01$ m, and $\Delta t = 0.01$ s. The Courant–Friedrichs–Lewy number CFL $\equiv (L\Delta t)/(T_{\mathrm{SF}}\Delta x) = 1.64$ in the deeper region and 0.97 in the shallower one. The polynomial order $N_T = 7$ is chosen.

In Fig. 2, the time series of the measured horizontal velocity $\bar{u}(z_0)$ and acceleration $\bar{ax}(z_0)$ (evaluated from $u(z_0)$ with a finite difference method in time) at different locations are displayed and compared with the simulated results. Here, $\bar{u}(z_0)$ and $\bar{ax}(z_0)$ denote the time series of $u(z_0)$ and $ax(z_0)$ normalized by the root-mean-square of the corresponding signal. Note that the measured and simulated time series need to be aligned at each location by introducing slightly different time shifts. This could result from three sources: (i) the measurements of $u(z_0)$ did not start at the same time in different repetitions of run 3; (ii) different wave propagation velocities (dispersion characteristics) in the numerical and experimental flumes; (iii) small error in the installation locations of the ADV device. Thus, the phase shift due to different dispersion characteristics alone cannot be directly evaluated. We anticipate that the phase shift due to the differences in wave velocity is small. This is because the agreement in the magnitudes of horizontal velocity and acceleration is quite good. Therefore, the nonlinear dispersion effects should be well captured by the model.

In the experiment, the horizontal velocity $u(z_0)$ was measured at 33 locations in the range $x \in [-0.45, 3.6]$ m, with the first measuring location set over the up-slope. In our simulations, we extend this range to $x \in [-2, 3.6]$ m by computing wave kinematics at 15 additional locations to track the "complete" evolution of kinematics as waves propagate over the shoal.

2.3. Wave kinematics computation validation for run 3 of Trulsen et al. (2020)

The spatial evolution of the frequency spectrum of $u(z_0)$ is shown in Fig. 3, with the measured one in panel (a) and the simulated one in panel (b). To better demonstrate the evolution of harmonics with relatively low amplitudes, $\log_{10}(S(f))$ is plotted in Fig. 3. In Fig. 3(b), the spectral evolution of simulated $u(z_0)$ in the spatial range $x \in [-2, -0.45]$ m is displayed as well, although no corresponding measurement is available in this range. It is observed that the simulated and measured spectra are in good agreement. In Fig. 5 of Zhang and Benoit (2021) it was noticed that the spectrum of η shows a beating pattern around $2f_p$ (due to the interaction between second-order free and bound harmonics). However, such a beating pattern is not so evident in the spectrum of $u(z_0)$. In Fig. 3(b), it is observed that the shoal starts to influence the spectral shape of $u(z_0)$ in a short distance after the beginning of the slope. The second-order harmonics in the spectrum of $u(z_0)$ are noticeably enhanced in the middle of the bar crest. The low-frequency components of $u(z_0)$ are also enhanced over the bar. As waves leave the bar crest and propagate over the de-shoaling zone, the spectrum of $u(z_0)$ gradually recovers a shape close to the one it had before encountering the bar.

The statistical parameters, skewness, asymmetry, and kurtosis indicate the magnitude of wave nonlinearity, and they are defined as:

$$\lambda_3(\bar{X}) = \left\langle \bar{X}^3 \right\rangle, \tag{2}$$

$$\lambda_3[\mathcal{H}(\bar{X})] = \left\langle \mathcal{H}(\bar{X})^3 \right\rangle, \tag{3}$$

$$\lambda_4(\bar{X}) = \left\langle \bar{X}^4 \right\rangle. \tag{4}$$

where $\langle\cdot\rangle$ denotes a mean operator, $\bar{X}$ denotes the random variable with zero mean and unit standard deviation, and $\mathcal{H}(\cdot)$ is the Hilbert transform operator. Here $\bar{X}$ could be normalized FSE, velocity, or acceleration. In particular, the kurtosis of FSE is frequently used as a proxy of freak wave probability. The extreme values in the time series of velocity and acceleration are related to extreme forces on structures, thus the statistical parameters of the particle kinematics below the free surface are of interest to engineers. Fig. 4 shows the spatial evolution of skewness, asymmetry, and kurtosis of both measured (red curves) and simulated (black asterisks)

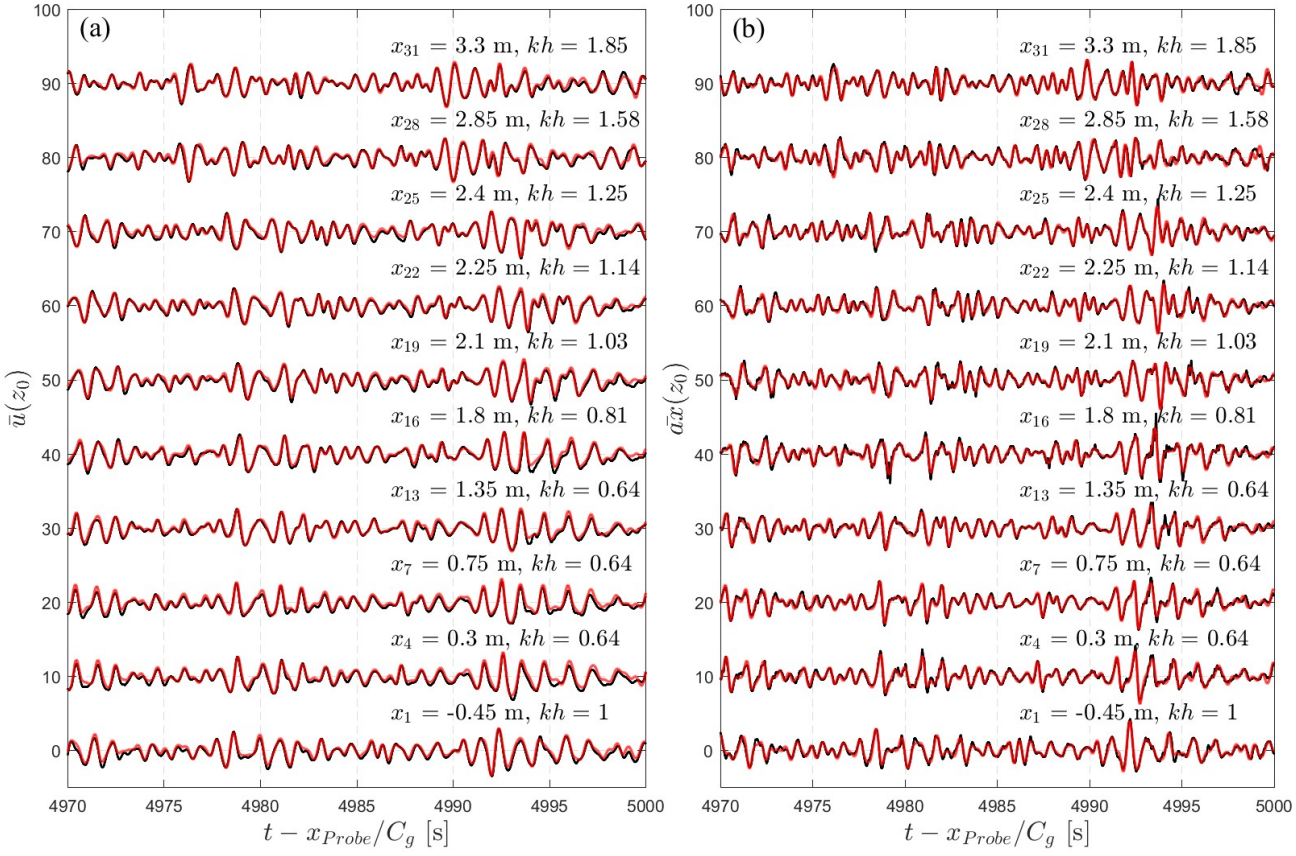

Figure 2: Normalized time series of the horizontal velocity $\bar{u}(z_0)$ (a) and horizontal acceleration $\bar{a}\bar{x}(z_0)$ (b) recorded along the wave flume in the simulation (red solid lines) and experiment (black dash lines).

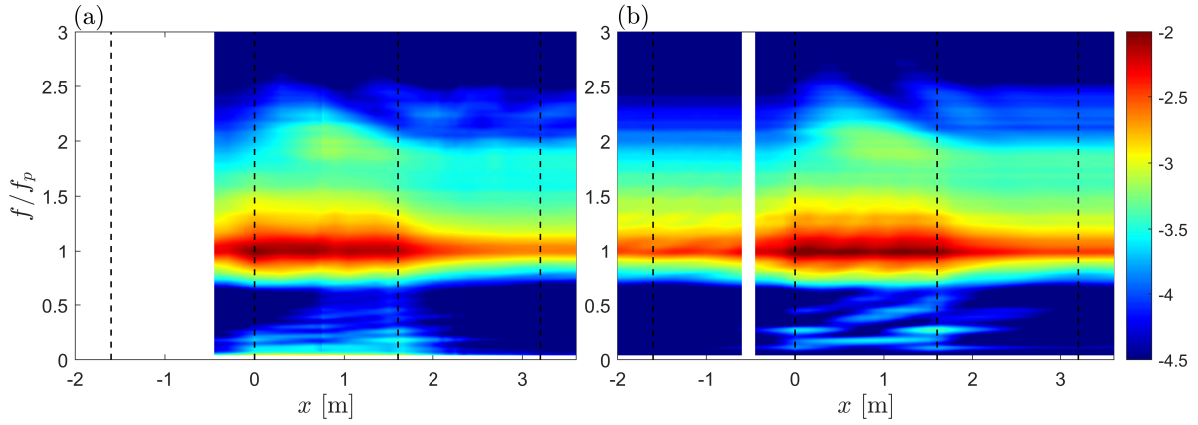

Figure 3: Spatial evolution of the spectrum of horizontal velocity $u(z_0)$ in the experiment (a) and in the simulation (b). The vertical dash lines indicate the extent of the submerged bar.

horizontal velocity $u(z_0)$ along the wave flume. Those of the simulated vertical velocity $w(z_0)$ (blue curves) are also displayed despite the lack of corresponding measurements. It is conjectured that the vertical velocity $w(z_0)$ is predicted with high fidelity, based on the excellent agreement achieved between simulated and measured $u(z_0)$ in both spectral and statistical domains.

In Fig. 4(a), the evolution trends of the skewness of $u(z_0)$ and $w(z_0)$ are similar to each other, yet the modulation of $\lambda_3[w(z_0)]$ in response to the depth variation develops faster in space than that of $\lambda_3[u(z_0)]$. Interestingly, it is noticed that, after the shoal, $\lambda_3[u(z_0)]$ achieves local extreme value when $\lambda_3[w(z_0)]$ vanishes, and vice versa. It indicates that the asymmetry (in the vertical direction) does not develop simultaneously for horizontal and vertical velocity components. In Fig. 4(b), the asymmetry parameter (indicating the velocity profile asymmetry in the horizontal direction) $\lambda_3[\mathcal{H}(u(z_0))]$ shows that the profile of $u(z_0)$ first leans back-

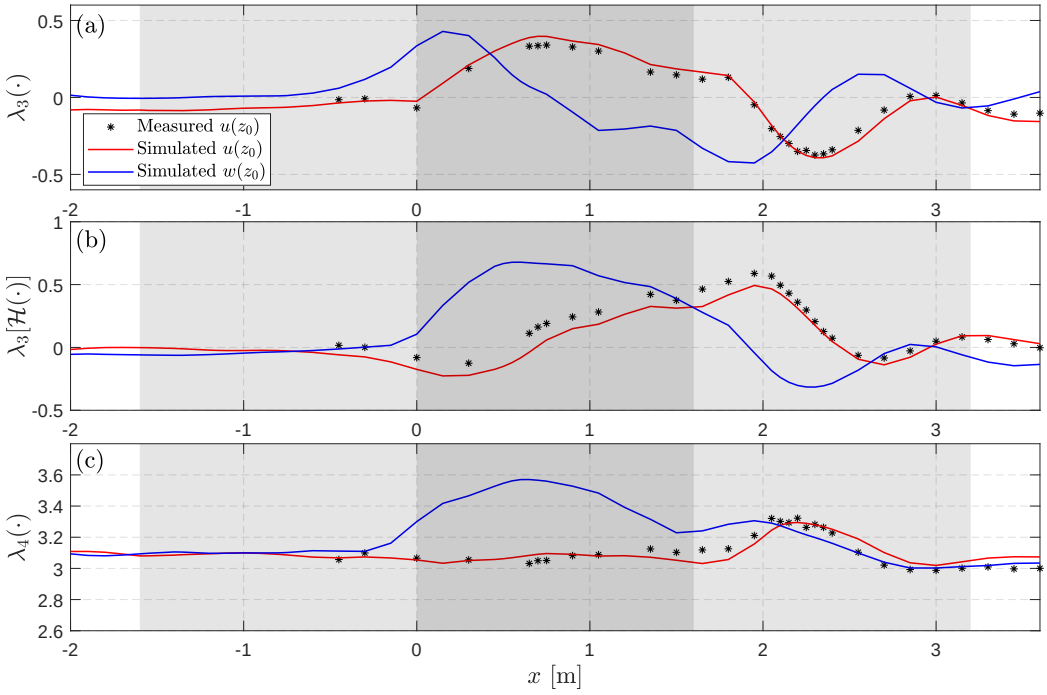

Figure 4: Spatial evolution of the statistical parameters of the horizontal velocity ($u(z_0)$) and the vertical velocity ($w(z_0)$), skewness is shown in panel (a), asymmetry parameter in panel (b) and kurtosis in panel (c). The gray areas indicate the extent of the submerged bar.

ward and then forward while, on the contrary, the profile of $w(z_0)$ first leans forward then backward in an averaged sense. For the kurtosis in Fig. 4(c), $\lambda_4[w(z_0)]$ achieves its global maximum over the bar crest whereas $\lambda_4[u(z_0)]$ is more or less unchanged over the bar and is locally enhanced over the down-slope area due to the de-shoaling effect, as it has been pointed out in Trulsen et al. (2020) and explained in Zhang and Benoit (2021).

Fig. 5 compares the spectral evolution of measured (in panel a) and simulated (in panel b) $ax(z_0)$. It is observed that in comparison to the spectral evolution of $u(z_0)$ shown in Fig. 3, the second-order harmonics are more evident, and the beating pattern is present in the spectral evolution of acceleration. This can be explained by the linear theory, the modulus of the particle acceleration is ω times the particle velocity at the same location, thus the amplitudes of the high-frequency harmonics are larger compared to the velocity. Note that the "beating pattern" mainly appears around $2f_p$, it is anticipated that the beating in higher harmonics does not manifest because of the presence of the de-shoaling area. In Fig. 5, it is seen that the low-frequency components are of low amplitudes such that they are not visible with the current colour scale. This is again in agreement with linear theory, for long waves with $\omega < 1$ rad/s at this scale, the acceleration moduli are smaller in comparison to the ones of the velocities. The good agreement between the measured and the simulated acceleration spectra in Fig. 5 shows the high fidelity of W3D for computing particle acceleration below strongly nonlinear irregular waves.

Fig. 6 displays the spatial evolution of statistical parameters of both horizontal and vertical accelerations, with skewness shown in panel (a), asymmetry parameter in panel (b), and kurtosis in panel (c). As a general remark, the statistical parameters of the simulated results are in excellent agreement with those of the measured data. Only some minor underestimations of the second local peak of kurtosis (around $x = 1.9$ m) are observed. The simulated statistical parameter evolution of $ax(z_0)$ seems to agree better with the measurements than that of $u(z_0)$. It is possibly related to the fact that the differences between the simulation results and the measurements in low-frequency components are reduced for $ax(z_0)$, as indicated in Fig. 5. The statistical parameters of the vertical acceleration $az(z_0)$ are superimposed in Fig. 6, despite the lack of corresponding measurements. The skewness $\lambda_3(az(z_0))$ is negative over the bar crest indicating a strongly skewed probability distribution, and the kurtosis $\lambda_4(az(z_0))$ achieves its global maximum value of about 5.4 shortly after the shoal and is much higher than that of $ax(z_0)$.

3. Statistical distribution of nonlinear irregular wave kinematics

3.1. Positive and negative log-normal distribution

Now we focus on the statistical distribution of water particle kinematics. Within the linear framework, both velocity and acceleration should follow the Gaussian (G) distribution. The wave nonlinearity would result in non-Gaussian characteristics in the distributions. Recently, Zhang et al. (2024) introduced a new distribution model of FSE of log-normal shape, which shows very good performance in the statisti-

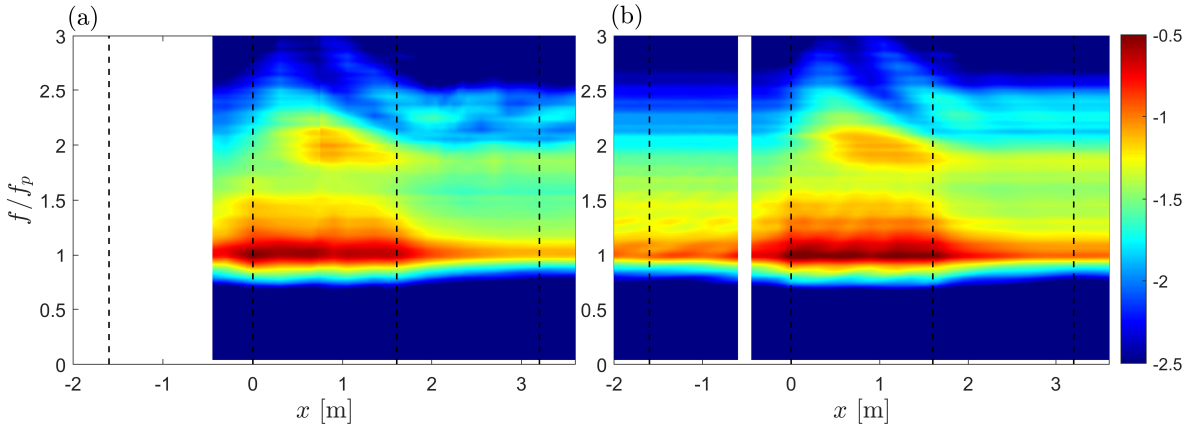

Figure 5: Spatial evolution of the spectrum of horizontal acceleration $ax(z_0)$ in the experiment (a) and in the simulation (b). The vertical dash lines indicate the shape of the submerged bar.

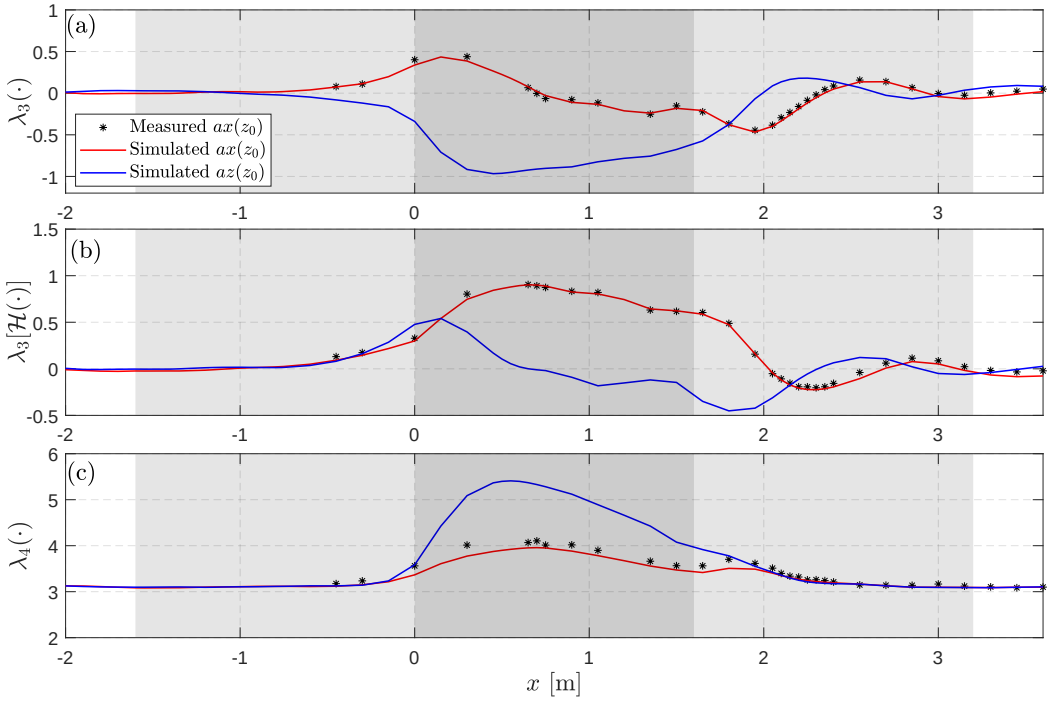

Figure 6: Spatial evolution of the statistical parameters of the horizontal acceleration ($ax(z_0)$) and the vertical acceleration ($az(z_0)$), skewness is shown in panel (a), asymmetry parameter in panel (b) and kurtosis in panel (c). The gray areas indicate the submerged bar.

cal description of waves propagating over a submerged step bottom. For completeness, we recall the definition and some properties of the LN model.

The LN distribution is fully determined by three parameters: a location parameter a_p, a scale parameter a_s, and a shape parameter τ. The standard LN model of a random variable X is defined by:

$$p_{LN}(X) = \frac{1}{\left(X - a_p\right)\tau\sqrt{2\pi}} \exp\left(-\frac{\left[\ln\left(X - a_p\right) - a_s\right]^2}{2\tau^2}\right) \tag{5}$$

over the range $X \in (a_p, +\infty)$, which we also call the "positive LN model" as the positive tail extends to $+\infty$. When $X \sim \mathrm{LN}(a_p, a_s, \tau^2)$, one can easily verify that the random variable $Z := \ln\left(X - a_p\right)$ follows the G distribution, $Z \sim \mathrm{G}(a_s, \tau^2)$. When the shape parameters $\tau \to 0^+$, the LN model tends to the G model. From now on, let us assume that $\tau > 0$ and define $q(\tau) \equiv \exp(\tau^2) > 1$. The first four statistical moments of the distribution (5) can be obtained analytically:

$$\langle X \rangle = a_p + \sqrt{q}\, e^{a_s}, \tag{6}$$

$$\sigma(X) = e^{a_s}\sqrt{q(q-1)}, \tag{7}$$

$$\lambda_3(X) = (q+2)\sqrt{q-1}, \tag{8}$$

$$\lambda_4(X) = 3 + (q-1)\left(q^3 + 3q^2 + 6q + 6\right) \tag{9}$$

which shows that both the skewness λ_3 and the excess kurtosis $\lambda_{40} \equiv \lambda_4 - 3$ are both strictly positive as soon as $q > 1$, i.e. $\tau > 0$. In practice, the 3 parameters of model (5) can be determined from the mean, standard deviation and skewness of the empirical distribution using eqs. (6-8). Furthermore, as we work here with a normalized variable $\bar{X} \equiv \left(X - \left\langle \bar{X} \right\rangle\right)/\sigma(X)$, implying $\left\langle \bar{X} \right\rangle = 0$ and $\sigma(\bar{X}) = 1$, we obtain from eqs. (6-7):

$$a_p = -\frac{1}{\sqrt{q-1}}, \tag{10}$$

$$a_s = -\frac{1}{2}[\ln q + \ln(q-1)], \tag{11}$$

showing that the location parameter a_p (i.e. the lower bound of the definition range of $\bar{X}$) is finite and strictly negative. All 3 parameters of model (5) for a normalized random variable are thus functions of the sole parameter q, which can be computed from the skewness solving a cubic polynomial equation from eq. (8). This yields:

$$q(\lambda_3) = \left[1 + \frac{\lambda_3}{2}\left(\lambda_3 + \sqrt{\lambda_3^2+4}\right)\right]^{1/3} + \left[1 + \frac{\lambda_3}{2}\left(\lambda_3 - \sqrt{\lambda_3^2+4}\right)\right]^{1/3} - 1 \tag{12}$$

Another interest of the LN model is that the kurtosis can be computed from eq. (9) once q is known, i.e. from the knowledge of the skewness solely. That is, the LN model possesses an intrinsic (fixed) Skewness–Kurtosis (S–K) relationship, deduced from eqs. (8-9):

$$\lambda_{40} = \lambda_4 - 3 = \frac{q^3 + 3q^2 + 6q + 6}{q^2 + 4q + 4}\lambda_3^2 \tag{13}$$

with $q(\lambda_3)$ given by eq. (12). This relation is explicit yet cumbersome. It can be approximated by noticing that q varies in a limited range above 1: when λ_3 increases from 0 (Gaussian case) to 1.5 (which is a quite large upper bound considering the results shown in Figures 4(b) and 6(b)), q increases from 1 to 1.217 approximately. Consequently, introducing $\delta \equiv q - 1 << 1$, eq. (13) can be reformulated as:

$$\frac{\lambda_{40}}{\lambda_3^2} = \frac{16 + 15\delta + 6\delta^2 + \delta^3}{9 + 6\delta + \delta^2}, \tag{14}$$

$$= \frac{16}{9}\frac{1 + \frac{15}{16}\delta + \frac{3}{8}\delta^2 + \frac{1}{16}\delta^3}{1 + \frac{2}{3}\delta + \frac{1}{9}\delta^2}, \tag{15}$$

and then approximated as:

$$\frac{\lambda_{40}}{\lambda_3^2} \approx \frac{16}{9}\left(1 + \frac{13}{48}\delta + \frac{1}{12}\delta^2 - \frac{5}{216}\delta^3\right). \tag{16}$$

It is remarkable that, at leading order, the S–K relationship of the LN model exactly matches the S–K relationship $\lambda_{40} = \frac{16}{9}\lambda_3^2$ derived by Mori and Kobayashi (1998) from a model of second-order in wave steepness. Furthermore, the dependency of the right-hand-side of eq. (16) in λ_3 is weak over the usual range of λ_3: taking again $\lambda_3 = 1.5$ as an indicative upper bound, one finds that the term in brackets in eq. (16) does not exceed 1.063. This closeness with the S–K relation of Mori and Kobayashi (1998) can be regarded as another advantage of the LN model, as recently shown in Zhang et al. (2024) for the FSE statistics in variable depth conditions.

However, we notice that the above "positive" LN model, adopted for FSE distribution in Zhang et al. (2024), is limited to non-negative skewness (due to the nature of eq. (8)). The FSE is generally of positive skewness (Longuet-Higgins, 1963), whereas the signal of velocities and accelerations are sometimes characterized by negative skewness (see e.g. Figs. 4(b) and 6(b)). We accommodate that by reversing the sign of the signal (which consequently reverses the sign of skewness) and then by flipping the obtained distribution, the LN distribution can then be used to describe random processes with negative skewness (therefore called "negative" LN distribution). With this simple manipulation of the signal, the LN distribution can not only be used for the FSE but also for the fluid kinematics underneath.

In the following, the statistical distributions of both measured and simulated FSE/velocity/acceleration at eight positions are displayed, and compared with the G distribution (as a linear expectation) and the LN distribution (as a nonlinear prediction). The chosen locations are considered representative, as they locate in the shoaling area ($x = -0.45$ m, and $x = 0$ m which is the end of the up-slope), over the bar crest ($x = 0.65$ m, $x = 0.75$ m, $x = 1.05$ m and $x = 1.5$ m), in the de-shoaling area ($x = 2.2$ m), and after the submerged bar ($x = 3.6$ m). It should be mentioned that the LN distribution can be built based on either the measured skewness or the simulated one. Here we adopt the measured skewness for the distribution of FSE, and the simulated skewness for the distributions of velocity and acceleration. The latter is chosen because the simulated results of velocity and acceleration cover a longer spatial extent than in the measurements. Furthermore, the vertical components of velocity and acceleration are available from simulations only for validating the LN model. We confirm that such a choice does not significantly differ from using the other way around, as the skewness of FSE/velocity/acceleration is reproduced in the simulation with high accuracy, as shown previously.

3.2. Distribution of FSE

In Fig. 7, it can be seen that the empirical PDF of the measured FSE is close to the Gaussian distribution in panel (a), the non-Gaussianity gradually develops when waves propagate over the shallower region, as shown in panels (b–d). Then the deviation of the empirical PDF from Gaussianity reduces when waves further propagate over the bar and the de-shoaling area, as shown in panels (e–h). Overall, the empirical PDFs of the measured and simulated FSE agree in a point-to-point manner, which was shown in Zhang and Benoit (2021). Interestingly, the LN model proves capa-

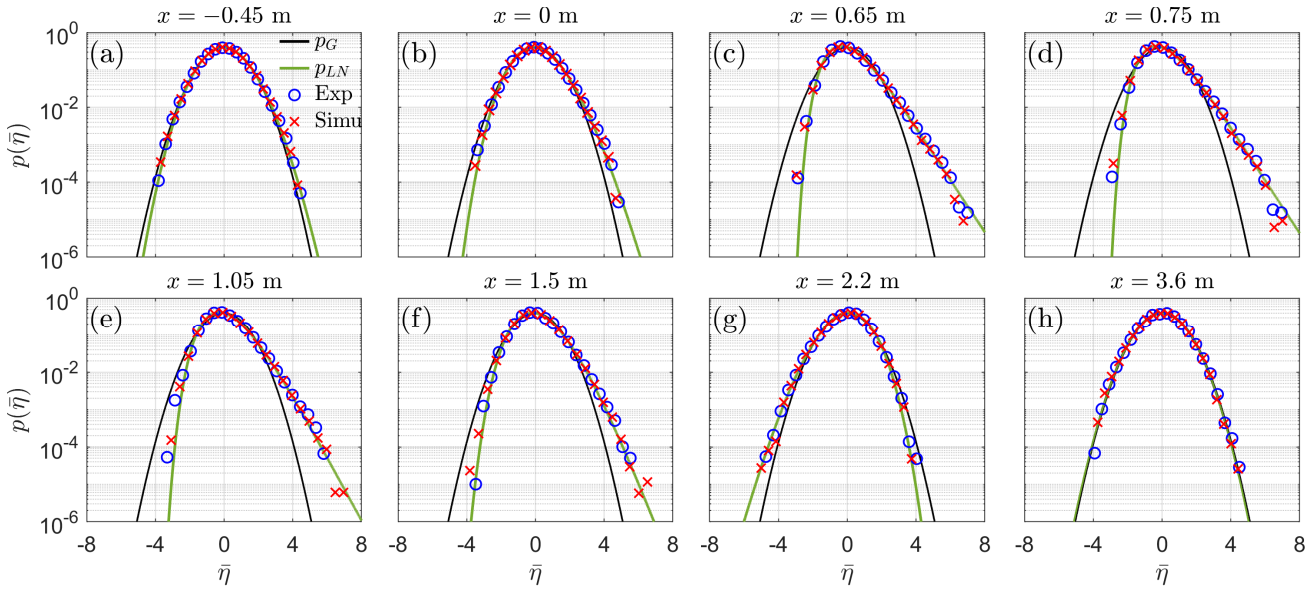

Figure 7: Empirical distribution of the measured and simulated FSE at eight locations along the wave flume, and the corresponding predictions of the G and LN distributions.

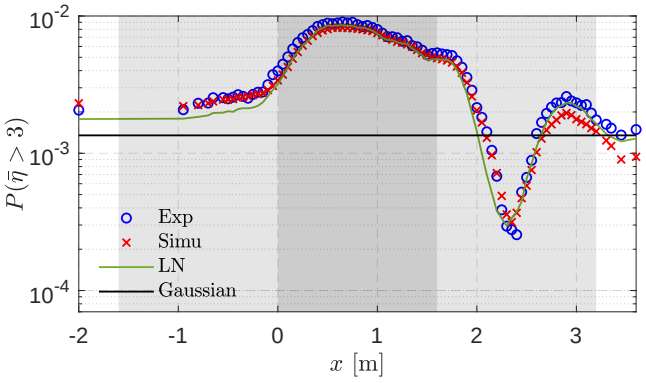

Figure 8: Spatial evolution of the exceedance probability for normalized FSE ($\bar{\eta}$) higher than 3. The gray areas indicate the submerged bar.

ble of accurately capturing the marked changes in empirical PDFs throughout the spatial domain.

To further illustrate the performance of the numerical model as well as the normal and LN distributions in predicting the empirical PDF of the measured and simulated FSE, the spatial evolution of the probability that the FSE exceeds a given level is analyzed. This level is set to 3 for $\bar{\eta}$ here, which means we consider $P(\bar{\eta} > 3)$ (with P denoting the exceedance probability function) or equivalently $P(\eta > 0.75 H_\sigma)$ where $H_\sigma \equiv 4\sigma(\eta)$ approximates the local significant wave height. Other exceedance levels could be considered similarly, the particular value of 3 is selected here as a balance between the wish to focus on the highest values of FSE and the need to keep a significant number of samples above that level in the empirical distributions. To put this value into perspective, according to the Gaussian distribution $P_G(\bar{\eta} > 3) \approx 1.35\,10^{-3}$. The evolution of $P(\bar{\eta} > 3)$ for all 91 probes displayed in Fig. 8 shows that both W3D and the LN model predict the tail part of the measured empirical FSE distribution with high accuracy. Good predictions are achieved not only for the near-equilibrium wave statistics before the shoal but also for the out-of-equilibrium wave statistics over the uneven seabed region. The black solid line represents the Gaussian prediction, which is a constant for all positions. The values of measured and predicted (by numerical simulation and LN model) $P(\bar{\eta} > 3)$ are higher than the prediction of normal distribution in the shallower flat region by a factor of 6.7 approximately, then lower in de-shoaling area. After the de-shoaling area, $P(\bar{\eta} > 3)$ seems to recover the prediction of the normal distribution.

3.3. Distributions of orbital velocities at $z_0 = -0.048$ m

Figs. 9 and 10 show the empirical/normal/LN distributions of particle velocity at $z_0 = -0.048$ m in horizontal and vertical directions, respectively. Fig. 10 shows only the empirical PDF of simulated vertical velocity $\bar{w}$ due to the lack of corresponding measurements. In Fig. 9, the PDF of $u(\bar{z}_0)$ from the simulation is in excellent agreement with that from measurements. Both empirical PDFs deviate from the normal distribution over the bar crest yet the deviations are not as significant as in the empirical distributions of $\bar{\eta}$. The LN distribution shows good performance in general, despite some minor overestimation of the largest positive values at $x = 0.65$ m and 0.75 m. In Fig. 10, the LN distribution predicts the empirical PDF of the simulated $\bar{w}$ quite well in general. However, at $x = 0.65$ m and 0.75 m where $\lambda_3(\bar{w}) \sim 0$, the empirical PDFs are indeed symmetric with respect to $\bar{w} = 0$ but are slightly higher than the prediction of normal distribution on both sides. At these two locations, the LN distribution is very close to the normal distribution,

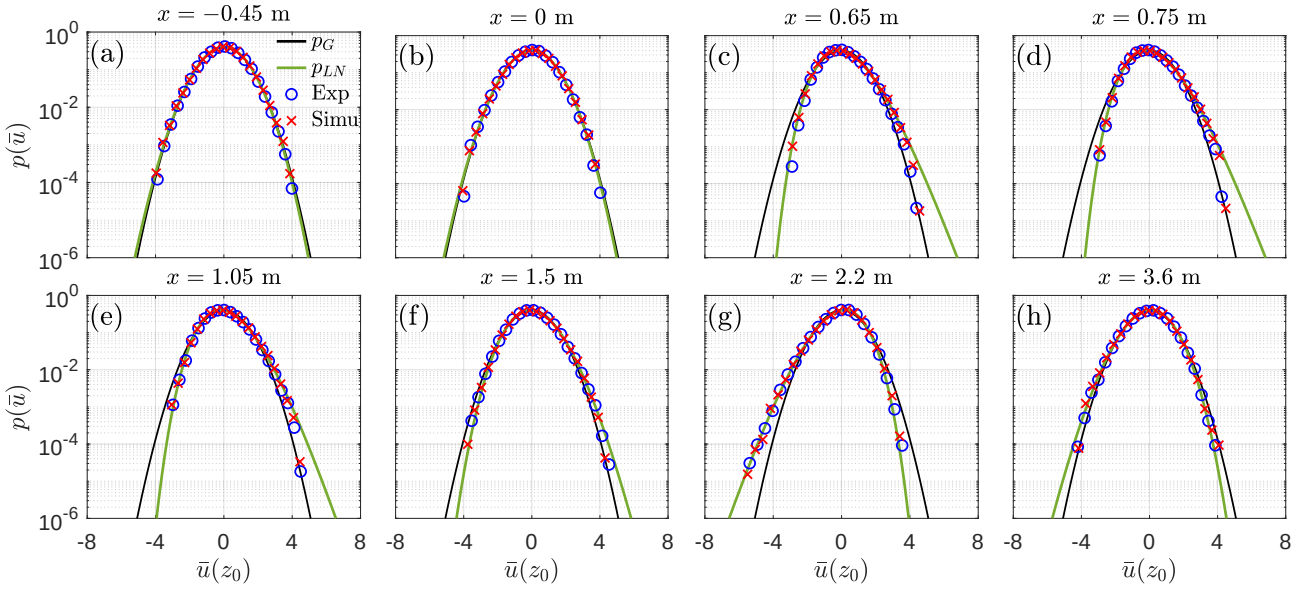

Figure 9: Empirical distribution of the measured and simulated horizontal velocity $\bar{u}(z_0)$ at $z_0 = -0.048$ m at eight locations along the wave flume, and the corresponding predictions of the G and LN distributions.

thus not capturing the non-Gaussian feature of the empirical distributions.

As for $\bar{\eta}$, the probabilities of $\bar{u}$ and $\bar{w}$ exceeding 3 are displayed for all locations where the velocities are measured or simulated. Fig. 11 shows the comparison of the exceedance probabilities of the empirical, normal, and LN distributions for the horizontal (in panel a) and the vertical velocity (in panel b). Again, the LN distributions are obtained based on the simulated skewness. The $P(\bar{u} > 3)$ in the measurement is well predicted by the LN distribution as well as the numerical simulation. However, for the simulated $P(\bar{w} > 3)$ shown in panel (b), the LN distribution under-predicts the exceedance probability. This under-prediction is related to the fact that the empirical distribution is symmetric yet higher than Gaussian prediction.

3.4. Distributions of Eulerian accelerations at $z_0 = -0.048$ m

The horizontal and vertical acceleration distributions are shown in Fig. 12 and 13 respectively, comparing the empirical PDFs with predictions of normal and LN models at eight locations. In Fig. 12, the change of horizontal acceleration distribution as waves propagate over the bar is evidently different from that of the FSE and the horizontal velocity. After entering the shallower flat region, the empirical PDF becomes non-Gaussian in the sense that the probability of both positive and negative $\bar{ax}$ are higher than Gaussian expectation. This feature is well captured by the numerical simulation, yet it is beyond the capability of the normal and LN distribution. In Fig. 13, the vertical acceleration probability is enhanced in the negative range of $\bar{az}$, which is related to its phase. The positive range of $\bar{az}$ is not as low as predicted by the LN distribution, but more or less in agreement with the normal distribution.

In Fig. 14, the exceedance probabilities of acceleration in both horizontal (panel a) and vertical (panel b) directions are displayed. As the vertical acceleration is mainly of negative skewness, $P(\bar{az} < -3)$ is shown instead of $P(\bar{az} > 3)$. In panel (a), the performance of the LN distribution for $P(\bar{ax})$ is acceptable but not as good as for other variables. This is again due to the non-Gaussian behaviour of the empirical distribution, which is symmetric but higher than Gaussian in both positive and negative ranges of $\bar{ax}$. In panel (b), the LN distribution captures well the evolution of $P(\bar{az} < -3)$.

To summarize, as random variables, the FSE, horizontal and vertical velocity, and acceleration, all follow the normal distribution when wave nonlinearity is insignificant. Non-Gaussian characteristics develop as waves propagate over the uneven bottom, and deviations from the normal distribution become clear. Our analyses show that, with the skewness of the random process given as an additional input, the LN distribution has great capabilities in describing random processes with evident non-Gaussian behaviour, especially for the abnormally high probability of large events. The LN distribution is quite general and can be applied not only for the FSE of nonlinear irregular waves but also for the particle kinematics underneath. The LN distribution has some limitations though, it cannot describe non-Gaussian statistical processes with symmetric PDF (i.e. with vanishing skewness but non-trivial kurtosis).

4. Conclusion

In this study, the statistics of particle kinematics underneath nonlinear irregular waves propagating over an uneven bottom were investigated experimentally and numerically. We adopted the new formulations of orbital velocities and accelerations in the FNPF wave model Whispers3D recently derived and validated in BZM2024. Here, the numerical model was further validated against experimental results of

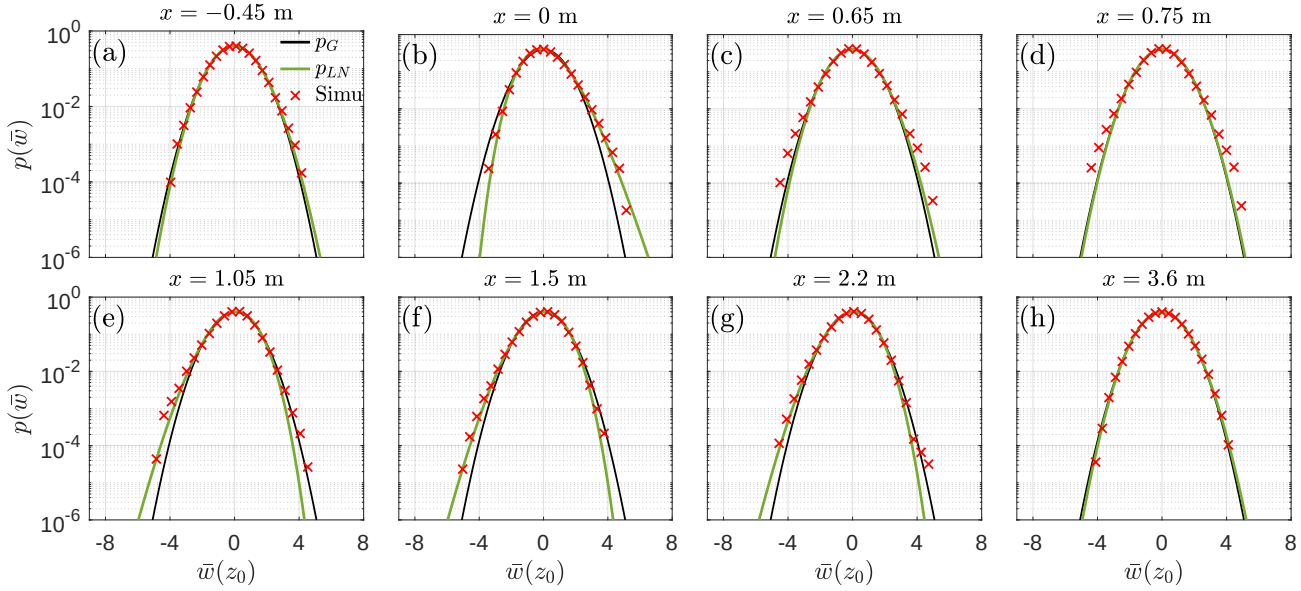

Figure 10: Empirical distribution of the simulated vertical velocity $\bar{w}(z_0)$ at $z_0 = -0.048$ m at eight locations along the wave flume, and the corresponding predictions of the G and LN distributions.

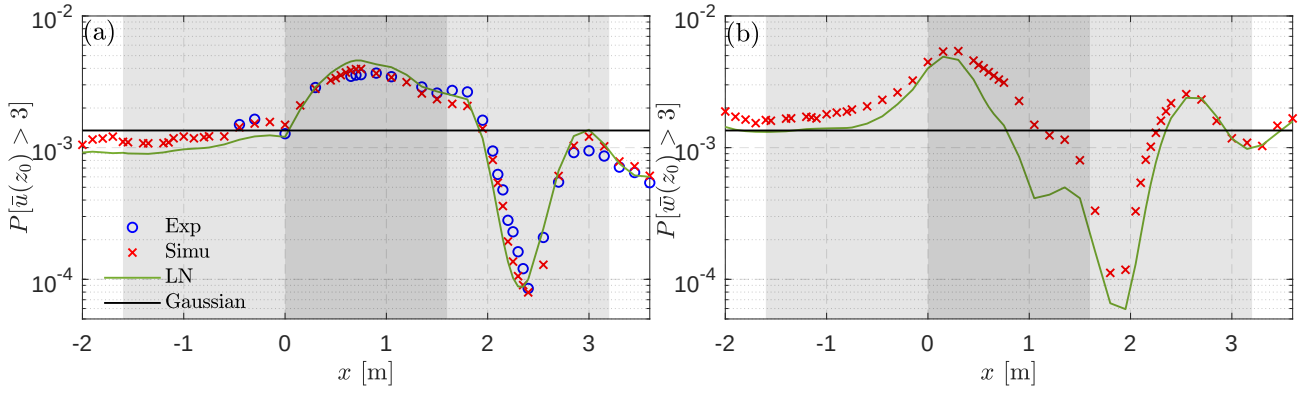

Figure 11: Spatial evolution of the exceedance probability for normalized horizontal velocity $\bar{u}(z_0)$ in panel (a) and vertical velocity $\bar{w}(z_0)$ in panel (b) higher than 3. The gray areas indicate the extent of the submerged bar.

the non-equilibrium wave evolution over a submerged bar with steep upslope and downslope reported in Trulsen et al. (2020). We chose Run 3 of the experiments as a high-quality measurement of the horizontal particle velocity below the FSE is available. Very good agreement is achieved in temporal, spectral, and statistical domains for simulated velocities and accelerations compared to the corresponding measurements. In particular, the W3D model simulates the non-equilibrium statistics variations (asymmetry, skewness and kurtosis) induced by the rapid changes in water depth over the shoal with high fidelity.

With the validated model, we then investigated the statistical distributions of particle kinematics for nonlinear irregular waves over the uneven bottom. Considering a long time series of about 5000 waves, the PDF of both experimental measurements and W3D simulations were built for the horizontal and vertical components of both velocity and acceleration. The simulated and measured empirical distributions are compared with the Gaussian (linear) and the log-normal (nonlinear) distributions. The latter was very recently proposed in Zhang et al. (2024) for positively skewed FSE signals. Here, it is adopted for negatively skewed signals by flipping the distribution. The key finding of this study is that the LN model is capable of describing most of the nonlinear features accompanying wave transformations in the shoaling and de-shoaling zones, including non-equilibrium effects. It represents the empirical distributions of FSE, velocities, and accelerations very accurately, indicating some generality of this model in describing the statistics of nonlinear wave processes. The LN model is particularly suitable for characterizing the heavy tail of the distributions, which is the primary interest in engineering applications. Another advantage lies in the fact that it possesses an intrinsic skewness-kurtosis (S–K) relationship (15), which we have shown here to be very close to the second-order relationship derived by Mori and Kobayashi (1998). Furthermore, we have provided a very

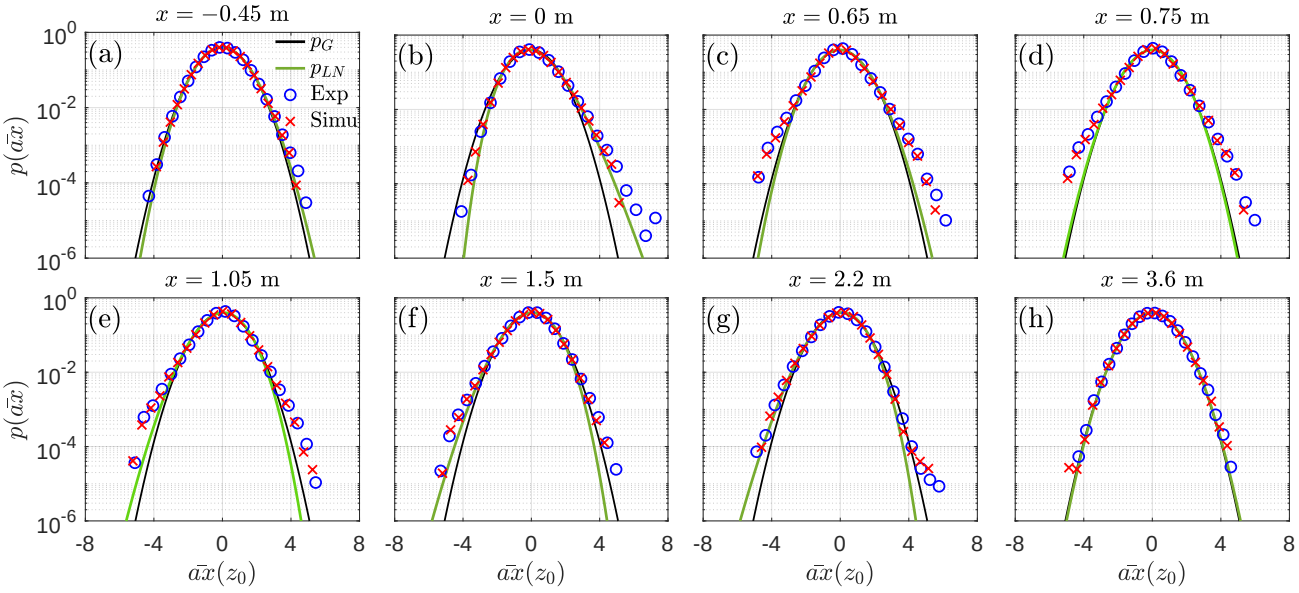

Figure 12: Empirical distribution of the measured and simulated horizontal acceleration $\bar{a}x(z_0)$ at $z_0 = -0.048$ m at eight locations along the wave flume, and the corresponding predictions of the G and LN distributions.

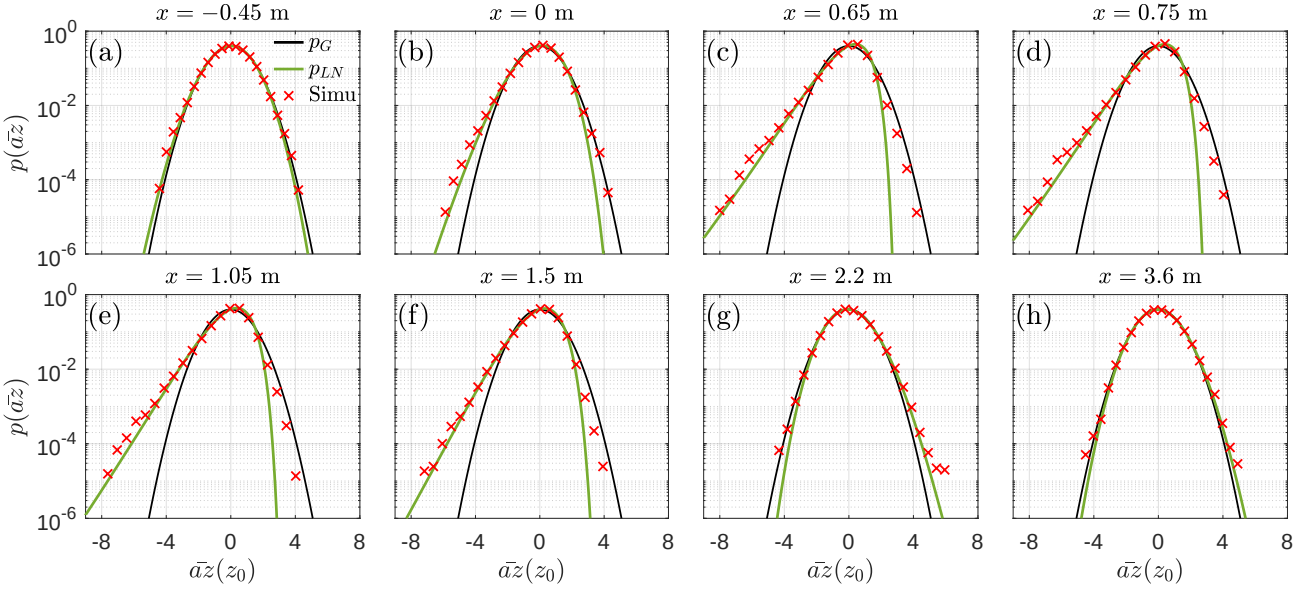

Figure 13: Empirical distribution of the simulated vertical acceleration $\bar{a}z(z_0)$ at $z_0 = -0.048$ m at eight locations along the wave flume, and the corresponding predictions of the G and LN distributions.

accurate approximation of this S–K relation (16) which allows a straightforward calculation of the kurtosis once the skewness is known (from either simulations or experiments).

As a next step of this work, in the spirit of Li et al. (2023), the model will be applied to the computation of nonlinear wave loads on marine structures in variable seabed conditions, in particular on slender structures for which a Morison-type approach can be used, e.g. monopiles for offshore wind turbines. Given that the LN model shows good generality in describing the heavy tail in the statistical distributions, it is worth trying to apply this model for predicting extreme wave load probability on structures. Additional validation of kinematics conditions will also be done in other conditions, in particular with multidirectional waves and multimodal seas. Besides, additional validations of the LN model against other laboratory and field measurements of FSE as well as the kinematics underneath have to be conducted, to better establish its capabilities and limitations.

CRediT authorship contribution statement

Jie Zhang: Funding acquisition, Investigation, Formal analysis, Writing – Original Draft. **Yuxiang Ma:** Resources, Writing – Review & Editing, Supervision. **Michel Benoit:**

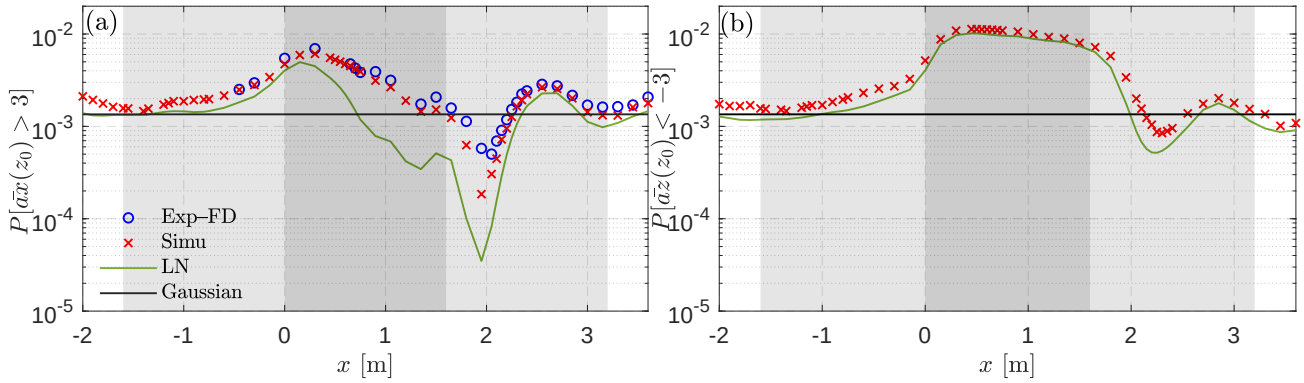

Figure 14: Spatial evolution of the exceedance probability for normalized horizontal acceleration $\bar{a}x(z_0)$ in panel (a) and vertical acceleration $\bar{a}z(z_0)$ in panel (b) higher than 3. The gray areas indicate the extent of the submerged bar.

Conceptualization, Methodology, Writing – Original Draft, Writing – Review & Editing, Supervision.

Declaration of competing interest

The authors declare that they have no known competing financial interests or personal relationships that could have appeared to influence the work reported in this paper.

Acknowledgments

This work was supported by the National Natural Science Foundation of China (Grant No. 52101301), and the China Postdoctoral Science Foundation (Grants No. 2023T160078, 2021M690523). The authors would like to express their gratitude to K. Trulsen, A. Raustøl, S. Jorde, and L.B. Rye for making their experimental dataset of Trulsen et al. (2020) open access.

References

Aggarwal, A., Chella, M.A., Kamath, A., Bihs, H., Arntsen, Ø.A., 2016. Irregular wave forces on a large vertical circular cylinder. Energy Procedia 94, 504–516. doi:10.1016/j.egypro.2016.09.223.

Benoit, M., Zhang, J., Ma, Y., 2024. Kinematics of nonlinear waves over variable bathymetry. Part I: Numerical modelling, verification, and validation. Coast. Eng. 193, 104577.

Bolles, C.T., Speer, K., Moore, M.N.J., 2019. Anomalous wave statistics induced by abrupt depth change. Phys. Rev. Fluids 4, 011801. doi:10.1103/physrevfluids.4.011801.

Bonar, P.A.J., Fitzgerald, C.J., Lin, Z., van den Bremer, T.S., Adcock, T.A.A., Borthwick, A.G.L., 2021. Anomalous wave statistics following sudden depth transitions: Application of an alternative Boussinesq-type formulation. J. Ocean Eng. Mar. Energy 7, 145–155. doi:10.1007/s40722-021-00192-0.

Deng, Y., Zhu, C., Wang, Z., 2023. A comparative study of wave kinematics and inline forces on vertical cylinders under Draupner-type freak waves. Ocean Eng. 288, 115959. doi:10.1016/j.oceaneng.2023.115959.

Didenkulova, E., Didenkulova, I., Medvedev, I., 2023. Freak wave events in 2005–2021: statistics and analysis of favourable wave and wind conditions. Nat. Hazards Earth Syst. Sci. 23, 1653–1663. doi:10.5194/nhess-23-1653-2023.

Didenkulova, E.G., Pelinovsky, E.N., 2020. Freak waves in 2011–2018. Dokl. Earth Sci. 491, 187–190. doi:10.1134/s1028334x20030046.

Didenkulova, I., Pelinovsky, E., 2016. On shallow water rogue wave formation in strongly inhomogeneous channels. J. Phys. A: Math. Theor. 49, 194001. doi:10.1088/1751-8113/49/19/194001.

Elfrink, B., Baldock, T., 2002. Hydrodynamics and sediment transport in the swash zone: a review and perspectives. Coast. Eng. 45, 149–167. doi:10.1016/s0378-3839(02)00032-7.

Fredsøe, J., Deigaard, R., 1992. Mechanics of Coastal Sediment Transport. Advanced Series on Ocean Engineering: Vol. 3. World Scientific. doi:10.1142/1546.

Freilich, M.H., Guza, R.T., 1984. Nonlinear effects on shoaling surface gravity waves. Philos. Trans. A: Math. Phys. Eng. Sci. 311, 1–41. doi:10.1098/rsta.1984.0019.

Fuhrman, D.R., Klahn, M., Zhai, Y., 2023. A new probability density function for the surface elevation in irregular seas. J. Fluid Mech. 970, A38. doi:10.1017/jfm.2023.669.

Goda, Y., 2010. Random seas and design of maritime structures, Third Edition. World Scientific Publishing Company.

Herrman, M.N., Kobayashi, N., Johnson, B.D., Orzech, M.D., 1997. Experiments on surface elevation probability distribution and statistics in surf and swash zones. Technical Report. Research Report No.CACR-97-01. Center for Applied Coastal Research, Ocean Engineering Laboratory, University of Delaware, Newark, Delaware, p. 127, 19716.

Klahn, M., Zhai, Y., Fuhrman, D.R., 2024. Heavy tails and probability density functions to any nonlinear order for the surface elevation in irregular seas. J. Fluid Mech. 985, A35. doi:10.1017/jfm.2024.304.

Kobayashi, N., Herrman, M.N., Johnson, B.D., Orzech, M.D., 1998. Probability distribution of surface elevation in surf and swash zones. J. Waterw. Port. Coast. 124, 99–107. doi:10.1061/(asce)0733-950x(1998)124:3(99).

Kriebel, D.L., 1998. Nonlinear wave interaction with a vertical circular cylinder: wave forces. Ocean Eng. 7, 597–605.

Lawrence, C., Gramstad, O., Trulsen, K., 2021. Variational Boussinesq model for kinematics calculation of surface gravity waves over bathymetry. Wave Motion 100, 102665. doi:10.1016/j.wavemoti.2020.102665.

Lawrence, C., Trulsen, K., Gramstad, O., 2022. Extreme wave statistics of surface elevation and velocity field of gravity waves over a two-dimensional bathymetry. J. Fluid Mech. 939, A41. doi:10.1017/jfm.2022.227.

Li, Y., Draycott, S., Zheng, Y., Lin, Z., Adcock, T.A.A., van den Bremer, T.S., 2021. Why rogue waves occur atop abrupt depth transitions. J. Fluid Mech. 919, R5. doi:10.1017/jfm.2021.409.

Li, Z., Tang, T., Li, Y., Draycott, S., van den Bremer, T.S., Adcock, T.A.A., 2023. Wave loads on ocean infrastructure increase as a result of waves passing over abrupt depth transitions. J. Ocean Eng. Mar. Energy 9, 309–317. doi:10.1007/s40722-022-00269-4.

Longuet-Higgins, M.S., 1952. On the statistical distributions of sea waves. J. Mar. Res. 11, 245–265. doi:citeulike:5677786.

Longuet-Higgins, M.S., 1963. The effect of non-linearities on statistical

distributions in the theory of sea waves. J. Fluid Mech. 17, 459–480. doi:10.1017/s0022112063001452.

Mori, N., Kobayashi, N., 1998. Nonlinear distribution of neashore free surface and velocity, in: Coast. Eng. Proc. (ICCE'1998), pp. 189–202. doi:10.1061/9780784404119.013.

Ochi, M.K., Wang, W.C., 1984. Non-Gaussian characteristics of coastal waves, in: Coast. Eng. Proc. (ICCE'1984), p. 35. doi:10.9753/icce.v19.35.

Ostrowski, R., Stella, M., Szmytkiewicz, P., Kapiński, J., Marcinkowski, T., 2018. Coastal hydrodynamics beyond the surf zone of the south Baltic sea. Oceanologia 60, 264–276. doi:10.1016/j.oceano.2017.11.007.

Shi, J., Feng, X., Toumi, R., Zhang, C., Hodges, K., Tao, A., Zhang, W., Zheng, J., 2024. Global increase in tropical cyclone ocean surface waves. Nat. Commun. 15, 174. doi:10.1038/s41467-023-43532-4.

Socquet-Juglard, H., Dysthe, K., Trulsen, K., Krogstad, H.E., Liu, J., 2005. Probability distributions of surface gravity waves during spectral changes. J. Fluid Mech. 542, 195. doi:10.1017/s0022112005006312.

Song, J., Wu, Y., 2000. Statistical distribution of water-particle velocity below the surface layer for finite water depth. Coast. Eng. 40, 1–19. doi:10.1016/s0378-3839(99)00062-9.

Stansberg, C.T., Huse, E., Krokstad, J.R., Lehn, E., 1995. Experimental study of non-linear loads on vertical cylinders in steep random waves, in: Proc. 5th Int. Ocean Polar Eng. Conf. (ISOPE'1995), The Hague, The Netherlands, 11-16 June 1995, pp. ISOPE–I–95–013.

Sultan, N.J., Hughes, S.A., 1993. Irregular wave-induced velocities in shallow water. J. Waterway Port Coast. Ocean Eng. 119, 429–447. doi:10.1061/(asce)0733-950x(1993)119:4(429).

Tayfun, M.A., Alkhalidi, M.A., 2020. Distribution of sea-surface elevations in intermediate and shallow water depths. Coast. Eng. 157, 103651. doi:10.1016/j.coastaleng.2020.103651.

Trulsen, K., Raustøl, A., Jorde, S., Rye, L.B., 2020. Extreme wave statistics of long-crested irregular waves over a shoal. J. Fluid Mech. 882, R2. doi:10.1017/jfm.2019.861.

Trulsen, K., Zeng, H., Gramstad, O., 2012. Laboratory evidence of freak waves provoked by non-uniform bathymetry. Phys. Fluids 24, 097101. doi:10.1063/1.4748346.

Vested, M.H., Carstensen, S., Christensen, E.D., 2020. Experimental study of wave kinematics and wave load distribution on a vertical circular cylinder. Coast. Eng. 157, 103660. doi:10.1016/j.coastaleng.2020.103660.

Wilson, J.F., 2002. Dynamics of Offshore Structures. Wiley.

Winterstein, S.R., Haver, S., 2015. Modeling shallow water waves: truncated Hermite models and the shallow wave routine, in: Proceedings of the ASME 34th InternationalConference on Ocean, Offshore and Arctic Engineering, St. John's, Newfoundland, Canada, p. 11.

You, Z., 2009. The statistical distribution of nearbed wave orbital velocity in intermediate coastal water depth. Coast. Eng. 56, 844–852. doi:10.1016/j.coastaleng.2009.04.005.

Zelt, J.A., Gudmestad, O.T., Skjelbreia, J.E., 1995. Fluid accelerations under irregular waves. Appl. Ocean Res. 17, 43–54. doi:10.1016/0141-1187(94)00019-j.

Zhang, J., Benoit, M., 2021. Wave–bottom interaction and extreme wave statistics due to shoaling and de-shoaling of irregular long-crested wave trains over steep seabed changes. J. Fluid Mech. 912, A28. doi:10.1017/jfm.2020.1125.

Zhang, J., Benoit, M., Kimmoun, O., Chabchoub, A., Hsu, H., 2019. Statistics of extreme waves in coastal waters: Large scale experiments and advanced numerical simulations. Fluids 4, 99. doi:10.3390/fluids4020099.

Zhang, J., Ma, Y., Benoit, M., 2024. Statistical distributions of free surface elevation and wave height for out-of-equilibrium sea-states provoked by strong depth variations. Ocean Eng. 293, 116645. doi:10.1016/j.oceaneng.2023.116645.

Zheng, Y., Lin, Z., Li, Y., Adcock, T.A.A., Li, Y., van den Bremer, T.S., 2020. Fully nonlinear simulations of unidirectional extreme waves provoked by strong depth transitions: The effect of slope. Phys. Rev. Fluids 5, 064804. doi:10.1103/physrevfluids.5.064804.